Chemical Engineering Journal 404 (2021) 126523

Contents lists available at ScienceDirect

Chemical Engineering Journal

journal homepage: www.elsevier.com/locate/cej

Tuning the electronic structure of AuNi homogeneous solid-solution alloy with positively charged Ni center for highly selective electrochemical CO_2 reduction

Jican Hao[a,1], Han Zhu[a,*,1], Youzhi Li[b], Pengxin Liu[c], Shuanglong Lu[a], Fang Duan[a], Weifu Dong[a], Yingying Lu[b], Tianxi Liu[a], Mingliang Du[a,*]

[a] Key Laboratory of Synthetic and Biological Colloids, Ministry of Education, School of Chemical and Material Engineering, Jiangnan University, Wuxi 214122, PR China
[b] College of Chemical And Biological Engineering, Zhejiang University, Hangzhou 310027, China
[c] Department of Chemistry and Applied Bioscience, ETH Zürich Vladimir Prelog Weg 2, 8093 Zürich, Switzerland

HIGHLIGHTS

- 1. AuNi alloy with positive charged Ni center were synthesized on electrospun CNFs.
- 2. AuNi with enhanced electronic interaction caused by the electron withdrawal from Au.
- 3. AuNi alloy exhibits a high CO selectivity with CO Faradaic efficiency of 92%.
- 4. AuNi alloy make the d-band center more positive and reduce the free energy barrier.
- 5. *In situ* technologies reveal the phase evolution and active sites for CO_2 reduction.

GRAPHICAL ABSTRACT

A concept of atom-polymer hybridization to design homogeneous AuNi solid-solution alloy nanoparticles with positively charged Ni center supported on electrospun carbon nanofibers as highly efficient CO_2RR catalysts have been demonstrated.

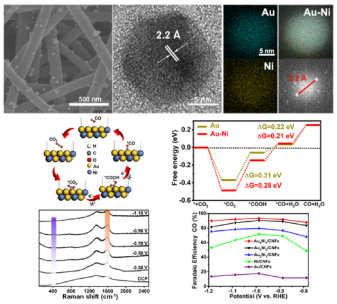

ARTICLE INFO

Keywords:
Carbon dioxide reduction
Homogeneous solid-solution alloy
Electronic structure
Electrospinning
Materials chemistry

ABSTRACT

Designing bimetallic electrocatalysts with homogenous element distribution and tunable electronic structure is attractive strategy to enhance the CO selectivity in electrochemical carbon dioxide reduction reaction (CO_2RR). Herein, we report a concept of atom-polymer hybridization to synthesize AuNi homogeneous solid-solution alloy nanoparticles (NPs) with positively charged Ni center supported on electrospun carbon nanofibers (CNFs). The nanofibers host can strong restrict the separated growth of Au and Ni nanoclusters during the directly graphitization process, leading to the formation of homogeneous AuNi alloy. *In-situ* characterizations reveal the formation process and phase evolution of the AuNi alloy during the carbonization. The positively charged Ni when alloying with Au lead to the enhanced local electronic structure on AuNi homogeneous solid-solution alloy due to the electron-withdrawal effect of nearby Au atoms. The AuNi homogeneous solid-solution alloy exhibits a high CO selectivity with an optimal CO Faradaic efficiency (FE_{CO}) of 92% at −0.98 V (vs. RHE). Theoretical calculations indicate that the incorporation of Ni into Au can make the *d*-band center more positive and reduce the

* Corresponding authors.
E-mail addresses: zhysw@jiangnan.edu.cn (H. Zhu), du@jiangnan.edu.cn (M. Du).
[1] J. Hao and H. Zhu contributed equally to this work.

https://doi.org/10.1016/j.cej.2020.126523
Received 5 May 2020; Received in revised form 30 July 2020; Accepted 31 July 2020
Available online 03 August 2020
1385-8947/

free energy barrier for the CO_2 activation into *COOH and *CO desorption. *Operando* Raman spectroscopy provides the evidences that AuNi homogeneous solid-solution alloy can facilitate the activation of CO_2 into *COOH and enhance the interaction between *COOH and AuNi (1 1 1) due to the change of electronic structure.

1. Introduction

The electrochemical reduction of carbon dioxide (CO_2RR) into value-added carbon products in aqueous electrolyte is a green and promising approach for energy conversion and carbon recycling [1,2]. Despite many efforts devoted to catalyst development, the competitive hydrogen evolution reaction (HER), multiple electron and proton transfer, excessive overpotentials, and poor selectivity in various products are still the major hurdles for further development of CO_2RR [3,4]. Hence, robust catalysts with high activity and particularly high selectivity for CO_2RR are highly desirable. Among the various target products, carbon oxide (CO) is regarded as significant product due to its important role as feedstock in chemical industry processes [5–8]. Noble metal (Au, Ag and Pd) [9–11] and transition metal (Ni, Sn and Fe) [3,12–14] and their alloy [10,12,15] have been widely used as CO_2RR electrocatalysts to obtain the CO products. However, the huge energy barrier for the activation of CO_2 on bimetallic alloy catalysts along with the inappropriate binding energy with CO_2RR intermediates and the inevitable HER in aqueous electrolytes resulting in the low Faradaic efficiency (FE) of CO (FE_{CO} < 50%) [16,17].

Alloying is a favorable strategy to enhance the activity of CO_2 reduction to CO on Au catalysts by optimizing the active sites for CO_2RR via the synergistic alloying effects including compositional effect [10,12], structural effect [12] and strain effect [15]. To our best knowledge, significant advances on noble metal bimetallic alloy nanoparticles (NPs) composed of miscible elements have been reported as high performance CO_2RR catalysts such as AuCu NPs, PdCu NPs and AuPd NPs [10,15,18,19], whereas there are rare researches on enhanced performance of CO_2 reduction to CO using supported solid-solution alloy NPs, because of the difficult preparation on solid-solution alloy NPs [12,13,15,18,20]. Recently, the supported Ni single atom catalysts containing the monovalent Ni(i) atomic center with positively charged states exhibits high intrinsic CO_2RR activity due to the unique electronic properties, suggesting that the electronic structures of catalysts play an important role in the CO_2 activation [5,21]. The alloying between Au and Ni could be an exciting approach for the design of efficient CO_2RR electrocatalysts. However, it is well known that the difficult fabrication of Au and Ni into solid-solution alloy according to bulk phase diagram [22]. The liquid phase synthesis for AuNi alloy usually obtains the phase-separated structure due to the different reduction kinetic of individual metal [23,24]. The electrodeposition method often results in the limited scope of AuNi alloy and the easy oxidization of Ni [25]. Meanwhile, direct heat treatment usually results in phase-segregated alloy with nonuniform composition distribution [26]. Therefore, the limited synthetic method still hinders the development of solid-solution alloy NPs as CO_2RR catalyst.

Recently, Hu and coworkers have reported the synthesis of high-entropy alloy NPs with homogeneous multi-element distribution on carbon support through the unique carbothermal shock method (CTS) [27]. The results indicate that the nanosize effect and surface defect can make the bulk-immiscible alloys transform into single phase alloy NPs. In addition, the extremely fast heating and cooling rates (10^5 k s^{-1}) suggests that the key factor for the synthesis of single-phase metal alloy with immiscible multiple elements is how to restrict the isolated growth of each elements. Solid-solution alloy composed of bulk-immiscible elements, the electronic structure can be continuously controlled by adjusting the composition of alloy, along with the change of catalytic activity. The reported CTS method exhibits the extreme conditions, including extremely high temperature (> 2000 K), and rapid heating and cooling (10^5 K s^{-1}), strongly limit researchers to monitor the synthesis process and control the elemental ratio and spatial arrangement. Therefore, it is important to develop a cost-effective synthetic route with good controllability over composition, size, morphology, and impurities.

As a proof-of-concept, we proposed the atom-polymer hybridization strategy for the synthesis of CNFs supported AuNi homogeneous solid-solution alloy NPs with positively charged Ni states and tunable local electronic structure by alloying the high-electronegativity Au metal as matrix with uniformly distributed Ni atoms. Electrospun polyvinyl pyrrolidone (PVP) nanofibers can host and confine the Au and Ni ions within the nanofiber matrix due to the strong coordination between the metal ion with carbonyl groups. During the graphitization process, the Au and Ni precursors in-situ decompose and form small NPs in the nanofiber reactor, and meanwhile, the internal stress of nanofibers caused by carbonization only allows for the localized nucleation and confined growth without drastic collision, leading to the formation of AuNi solid-solution alloy NPs with homogeneous mixing of elements. Synchrotron radiation X-ray absorption fine structure spectroscopy (XAFS) results strong confirmed the enhanced local electronic structure on AuNi homogeneous solid-solution alloy with positively charged Ni due to the electron withdrawal effect of nearby Au atoms. The AuNi solid-solution alloy supported on carbon nanofibers (AuNi/CNFs) were used as a self-supported CO_2RR electrode. The FE_{CO} and CO current density showed a dramatic increase when compared with the individual Au/CNFs and Ni/CNFs. The AuNi/CNFs with molar ratio for Au and Ni of 1:1 achieved a remarkable FE_{CO} of 92% at −0.98 V vs. RHE. Density functional theory (DFT) studies revealed that incorporation of Ni into Au makes the *d*-band center of AuNi (1 1 1) more positive and can tune the binding energies between metal and intermediates of CO_2RR. The AuNi homogeneous solid-solution alloy can significantly reduce the free energy barriers for the activation of CO_2 to *COOH and CO desorption, leading to the high CO selectivity. *Operando* Raman spectroscopy provided the evidences that AuNi homogeneous solid-solution alloy with positively charged Ni center can facilitate the activation of CO_2 into *COOH and enhance the interaction between *COOH and AuNi (1 1 1) due to the change of electronic structures. This work presents the general strategy for the synthesis of metal alloy nanostructures and demonstrates the understanding between the electronic structures and the adsorbed intermediates on catalyst surface during CO_2RR.

2. Materials and methods

2.1. Materials

Chloroauric acid ($HAuCl_4{\cdot}4H_2O$, 99.9%) was provided by Shanghai Civi Chemical Technology Co., Ltd. Nickel nitrate hexahydrate ($Ni(NO_3)_2{\cdot}6H_2O$, 99.9%) and dimethyl formamide (DMF, 99.5%) were commercially available from Sinopharm Chemical Regent Co., Ltd. Polyvinylpyrrolidone (PVP, $M_w \approx 1300000$) was manufactured by energy chemical Co., Ltd. All the chemicals were used directly without further purification.

2.2. Catalyst preparation

The Au-Ni-CNFs were prepared on the basis of previously published procedures. In a typical preparation, 4 mmol $HAuCl_4{\cdot}4H_2O$, 4 mmol $Ni(NO_3)_2{\cdot}6H_2O$ and 1.2 g PVP were sequentially dissolved in 10 g DMF under magnetic stirring for 5 h to obtain a homogeneous solution with the mass ratio of 30 wt% ($HAuCl_4{\cdot}4H_2O$ and $Ni(NO_3)_2{\cdot}6H_2O$ to PVP) at room temperature. Then, the prepared Au-Ni/PVP precursor solution

was directly injected into a 10 mL syringe equipped with a 24 gauge stainless steel needle at the tip. After that, the nanofibrous membranes were obtained by classical electrospinning method. The electrospinning parameters were as follows. The anode voltage was 15 kV and the distance between the needle tip and tin foil collector was 14 cm with the temperature and the humidity 25 ˚C and 30%, respectively. The flow rate and electrospinning period were 0.3 mL/h and 12 h, respectively. At last, the Au-Ni-CNFs was obtained by a graphitization treatment. The obtained electrospinning membrane was placed into a home-built chemical vapor deposition (CVD) system and was carbonized at setting temperature for 3 h under Ar atmosphere. After the CVD system was cooled down to the room temperature under an Ar atmosphere, the Au-Ni-CNFs was obtained. Here, we chose 800 ˚C, 900 ˚C and 1000 ˚C as the different setting temperatures. The prepared catalysts were named as Au_xNi_y/CNFs-z (prepared with conditions: molar ratios of $HAuCl_4{\cdot}4H_2O$: $Ni(NO_3)_2{\cdot}6H_2O$ = 1:3, 1:1 and 3:1, where "x and y" represents the molar ratio between $HAuCl_4{\cdot}4H_2O$ and $Ni(NO_3)_2{\cdot}6H_2O$, "z" donates the calcination temperatures: 800 ˚C, 900 ˚C and 1000 ˚C.). The controlled experimental catalysts were prepared in absence of metal salt with the similar process.

2.3. Catalyst characterization

Infrared spectra (IR) of the pure PVP electrospinning membrane and metal ions PVP composite films was obtained by using a Nicolet 6700 Fourier transform infrared (FTIR) spectrophotometer scanning from 500 to 4000 cm^{-1}. The ultraviolet-visible (UV–vis) spectra of the as-prepared PVP solution and metal ions PVP solution were examined by a UV-2700 (SHIMADZU, Japan). The morphological features analysis of as-prepared catalysts was carried out with a HITACHI S-4800 field emission scanning electron microscopy (FE-SEM) at an accelerating voltage of 3 kV. Transmission electron microscopy (TEM) images were performed using a JEM-2100 plus transmission electron microscope operated at 200 kV. The scanning transmission electron microscopy (STEM) images, energy dispersive X-ray spectroscopy (EDX) and STEM-EDX mapping were acquired with a STEM (Tecnai G2 F30s-Twin, Philips-FEI) operated at 200 kV. Aberration corrected transmission electron microscopy (ACTEM) images was carried out on modified FEI Themis TEM with a high-angle annular dark field (HAADF) detector operated at an accelerating voltage of 200 kV. Inductively coupled plasma optical emission spectrometry (ICP-OES) were performed on PerkinElmer 8300. The specific surface area was investigated using nitrogen with Quantasorb IQ using BET method at liquid nitrogen temperature (77 K). The pore size was calculated based on the Barrett − Joyner − Halenda (BJH) method using the desorption branches of nitrogen isotherms. The samples were outgassed under vacuum at 150 ˚C before the nitrogen-adsorption measurement. *In situ* XRD patterns of the sample was collected using an Empyrean100 diffractometer equipped with a high-temperature reaction cell (XRK 900, Anton Paar GmbH). The diffractometer was operated with a Cu K_α radiation source (λ = 1.5418 Å) at 40 kV and 40 mA. And *in situ* XRD patterns were recorded continuously with a 2θ range of 5 to 80˚ and a scanning rate of 0.02 2θ s^{-1}. The range of temperature was 400 ˚C to 1000 ˚C at a heating rate of 10 ˚C/min. X-ray diffraction (XRD) patterns were acquired by a Bruker AXS D8 instrument with Cu Kα radiation (λ = 1.5418 Å) at a scanning rate of 0.02 2θ s^{-1} in the 2θ range of 10-90˚. X-ray photoelectron spectroscopy (XPS) measurements were recorded using a Kratos Axis supra with with an aluminum (mono) K_α source (1486.6 eV). Ni K-edge absorption spectra (EXAFS) were performed on the 1W1B beamline at the Beijing Synchrotron Radiation Facility (BSRF) operated at 7 GeV with injection currents of 100 mA. The radiation was monochromatized by a Si (1 1 1) double-crystal monochromator. Ni foil and NiO were used as reference samples and measured in the fluorescence mode.

2.4. Catalyst measurement

The CO_2 electrochemical reduction reaction experiments were carried out on a three-electrode system with a gas-hermetic two 50 mL compartments H-cell at room temperature. Each compartment contains 40 mL CO_2-saturated 0.1 M $KHCO_3$ (pH = 6.8) as the electrolyte, holding 20 mL headspace. An anion-exchange membrane (Nafion 117) was used to separate two compartments containing working and counter electrodes. The prepared CNFs membrane was tailored into a neat square (0.5 × 0.8 cm^2) and directly fabricated as the working electrode. An Ag/AgCl electrode and a Pt wire were applied to the reference electrode and the counter electrode, respectively. All the electrochemical experiments were carried out on an Autolab 302 N electrochemical workstation. All measured electrode potentials in this experiment were converted to reversible hydrogen electrode (RHE) reference scale using E_{RHE} = E(vs Ag/AgCl) + $E_{Ag/AgCl}$ + 0.0591 × pH. After purging the electrolyte with N_2 or CO_2 gas for 30 min at a flow rate of 30 mL min^{-1}, the linear sweep voltammetry (LSV) was performed from 0 to − 2.0 V (vs. Ag/AgCl) at a scan rate of 50 mV s^{-1} to obtain the desired working potentials. Then, the electrolysis was conducted at each potential for 30 min, while the CO_2 was continuously bubbled into each compartment during the reduction experiment.

2.5. Product analysis

The gas products of working electrode compartment were analyzed by directly injected into the gas chromatograph (GC, Agilent 7890B), which was equipped with both the flame ionization detector (FID) for hydrocarbon gas product and thermal conductivity detector (TCD) for H_2. The experiment results indicated that the CO and H_2 were the only gas products. The electrolysis at each potential was repeated three times, and the average value of experiments was adapted as the gas concentration for Faradaic efficiency (FE) calculation. The Faradaic efficiency (FE) and the partial current densities (j_{CO} and j_{H2}) of CO and H_2 production were calculated as below. The liquid product existed in electrolyte was analyzed on a Bruker 400 MHz (AVANCE III) NMR spectroscope.

$$FE\% = Q_C O/Qtotal \times 100\% = ((v/(60s/\min)) \times (y/(24000cm^3/mol)) \times N \times F)/i \times 100\% \quad (1)$$

$$j_{co} = j \times FE_{Co} \quad (2)$$

where v is the flow rate of CO_2 (30 sccm), y is the concentration of the gas products (only CO and H_2 found in experiment) detected by GC with a standard gas, N is the number of transferred electrons for producing CO or H_2, which is 2 for CO and H_2, F is the Faradaic constant (96500C mol^{-1}), i is the measured current, j is the total current density.

2.6. DFT calculations

DFT calculations were performed in the Vienna ab initio simulation package (VASP). A spin-polarized GGA PBE functional, all-electron plane-wave basis sets with an energy cutoff of 520 eV, and a projector augmented wave (PAW) method were adopted. Au is simulated using a surface model of p (3 × 3) unit cell periodicity. A (3 × 3 × 1) Monkhorst-Pack mesh was used for the Brillouin-zone integrations to be sampled. The conjugate gradient algorithm was used in the optimization. The convergence threshold was set $1*10^{-4}$ eV in total energy and 0.05 eV/ Å in force on each atom.

In the simulations, non-periodic boundary condition is employed, and the molecular model of a pristine gold crystal with 41 Au atoms was established by using Materials Studio. Ni atoms doping in the gold structure were formed by replacing some Au atoms. To find the thermal stable morphology and achieve a conformation with minimum potential energy, energy minimization was performed. And these minimum

energy conformations were used as initial status in the following electronic structure simulations. The Visualization for Electronic and Structural Analysis (VESTA, series 3) and Materials Studio software were used for visualization and plotting.

The adsorption energy change (ΔE_{abs}) was determined as follows: [28]

$$\Delta E_{abs} = E_{total} - E_{sur} - E_{mol}$$

where E_{total} is the total energy for the adsorption state, E_{sur} is the energy of pure surface, E_{mol} is the energy of molecule.

The free energy change (ΔG) for adsorptions were determined as follows: [28]

$$\Delta G = E_{total} - E_{sur} + \Delta E_{ZPE} - T\Delta S$$

where E_{total} is the total energy for the adsorption state, E_{sur} is the energy of pure surface, ΔE_{ZPE} is the zero-point energy change and ΔS is the entropy change.

2.7. Operando Raman spectroscopy

Potential-dependent *Operando* Raman was performed using a Renishaw inVia confocal microscope (excitation wavelength 532 nm, power 3 mW on the sample), the Raman spectra of prepared catalysts were collected in a spectro-electrochemical cell, Ag/AgCl and Pt wire were used as reference electrode and counter electrode, respectively. Aqueous 0.1 M $KHCO_3$ was used as electrolyte. Electrochemical tests were operated on an Autolab 302 N electrochemical workstation. Raman spectroscopy was performed using the apparatus described in ref [29].

3. Results and discussion

3.1. Synthesis and structural characterizations of AuNi/CNFs catalysts

The AuNi homogeneous solid-solution alloy nanoparticles (NPs) supported on CNFs were prepared by combining the electrospinning technology and the graphitization treatment. As shown in Scheme 1a, the Au and Ni metal salt precursors were mixed with polyvinyl pyrrolidone/dimethyl formamide (PVP/DMF) solution. During the pre-oxidation stage at 230 °C, the metal salts began to decompose while the PVP nanofibers began to convert into amorphous carbon nanofibers. With further carbothermal reduction to 1000 °C, the surface tension difference between Au and Ni can be overcome. Meanwhile, the AuNi homogeneous solid-solution alloy NPs were thus formed confined by the PVP derived carbon nanofibers (CNFs). The liquid phase synthesis of AuNi alloy without polymer hybridization and the confinement effects from CNFs would lead to the intermetallic AuNi alloy with separated phase (Scheme 1b). Scheme 1c demonstrates the atom-polymer hybridization between the Au and Ni ions with the PVP chains. The direct evidences for the coordination acquired using Fourier-transform infrared spectroscopy (FT-IR) and ultraviolet–visible (UV–vis) spectroscopy (Scheme 1d). Compared with the FT-IR spectrum of PVP/DMF, the carbonyl (-C = O) adsorption peak of AuNi ions-PVP/DMF exhibit

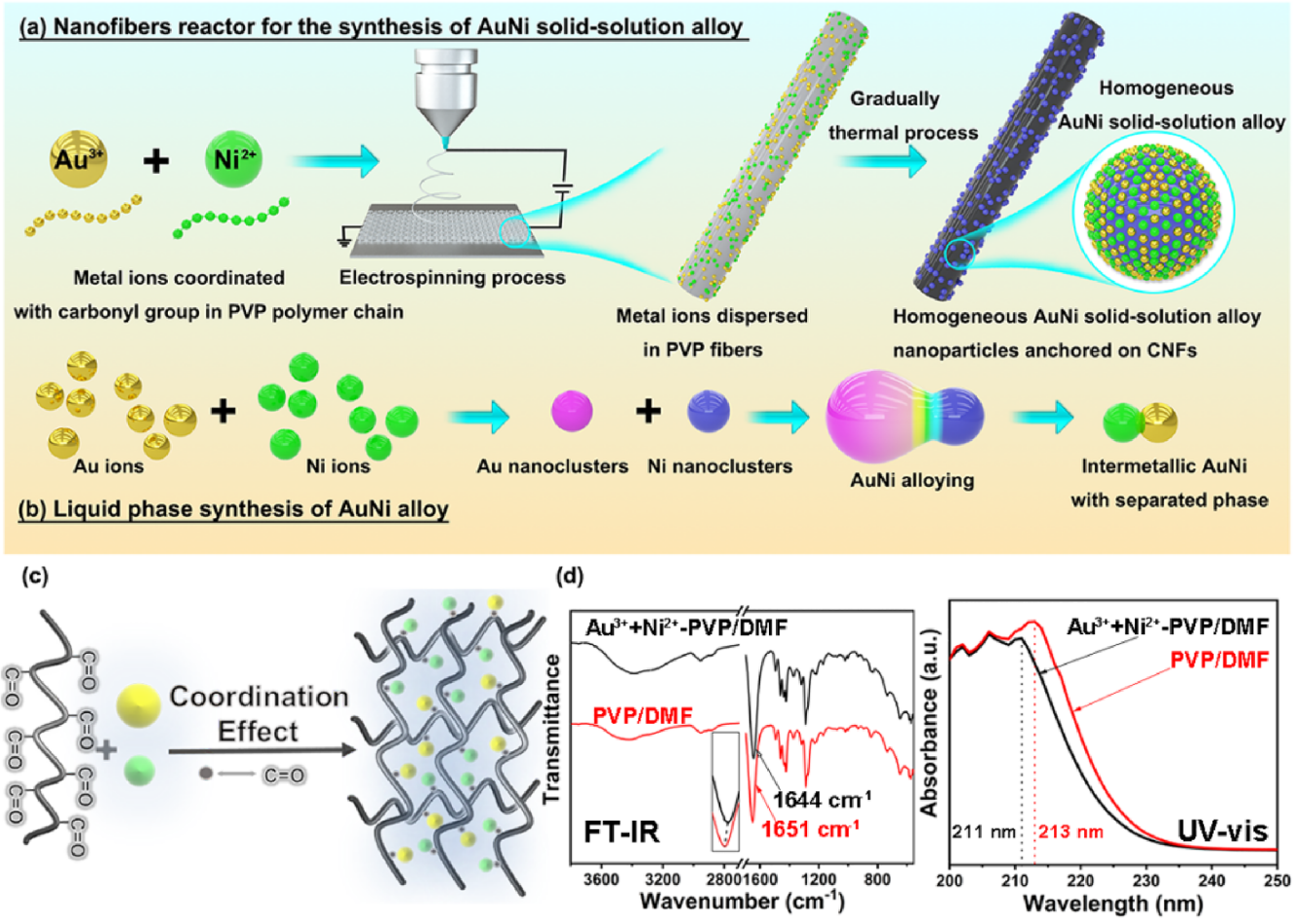

Scheme 1. (a) Scheme of the synthesis of the AuNi homogeneous solid-solution alloy. (b) Scheme for the liquid phase synthesis of AuNi homogeneous solid-solution alloy. (c) The schematic of the coordination effect between metal ions and PVP. (d) The FT-IR spectra and UV–vis spectra of the pure PVP nanofibers and AuNi salts/PVP nanofibers.

blue shift about 7 cm^{-1}. Similarly, the UV–vis spectrum demonstrates that the adsorption peak at 210 nm attributed to the carbonyl C = O groups in metal ions-PVP/DMF also display blue shifts about 3 nm in comparison with that of PVP. The results demonstrate the atom-polymer hybridization between the PVP and metal ions [30]. The structures and morphologies of the AuNi/CNFs prepared with different molar ratios of Au and Ni were shown in Fig. 1a-e. The individual Au/CNFs and Ni/CNFs were also prepared as control. Fig. 1a and 1f display that the uniform Au NPs with average size of about 10 nm are supported on PVP derived CNFs. High resolution transmission electron microscopy (HRTEM) image of Au/CNFs (inset in Fig. 1f) exhibits the distinct lattice fringes with an interlayer distance of 2.3 Å, corresponding to the (1 1 1) planes of face-centered cubic (*fcc*) Au phase [31].

The AuNi alloy NPs with different molar ratios are denoted as Au_3Ni_1/CNFs, Au_1Ni_1/CNFs and Au_1Ni_3/CNFs, respectively, which are shown in Fig. 1b-d and Fig. 1g-i. As shown in Fig. 1b-d, large amounts of the AuNi (Au_3Ni_1, Au_1Ni_1 and Au_1Ni_3) alloy NPs are densely distributed throughout the supported CNFs. The average diameter of the CNFs ranged from 150 to 200 nm and the nanofibers are distributed randomly, forming the three-dimensional (3D) continuous architecture, which would favor the mass diffusion and electron transfer during the electrochemical process. The total metal loading of the Au_1Ni_1/CNFs was 4 wt% examined by Inductively Coupled Plasma Optical Emission Spectrometer (ICP-OES, Table S1). In addition, the Au_1Ni_1/CNFs obtain a specific surface area of 582.5 $m^2\ g^{-1}$, suggesting that the 3D networks could benefit the CO_2 adsorption and transmission (Fig. S1). Interestingly, with increased Ni contents in molar ratio of Au and Ni from 3:1 to 1:3, the average sizes of the AuNi alloy NPs present a significant decreasing tendency from 14 to 5.5 nm (Fig. 1g-i, Fig. S2). The individual Ni/CNFs display uniform Ni NPs with small size about 8 nm (Fig. 1j). The results indicate that compared with the sizes of the individual Au (10 nm) and Ni (8 nm) NPs, the AuNi alloying would lead to the increased sizes and interestingly, the higher Ni contents in AuNi alloy lead to smaller sizes of the AuNi alloy NPs. It could be attributed to the stronger coordination effects between the Ni and carbon, which could further restrict the growth of AuNi alloy to larger sizes. Fig. 1k shows the aberration-corrected high-angle annular dark field scanning transmission electron microscopy (AC-HAADF-STEM) images of Au_1Ni_1/CNFs, the measured lattice distance of 2.2 Å corresponds to the (1 1 1) plane of AuNi solid-solution alloy NPs (Fig. S3) [32,33].

As shown in inset in Fig. 1j, the Ni/CNFs indicate a visible lattice fringe with *d* spacing of 2.0 Å, corresponding to the (1 1 1) plane of the Ni crystals. The *d* spacing value for (1 1 1) planes of the Au_1Ni_1 (2.2 Å) solid-solution alloy NPs between the Au (2.3 Å) and Ni (2.0 Å) NPs was

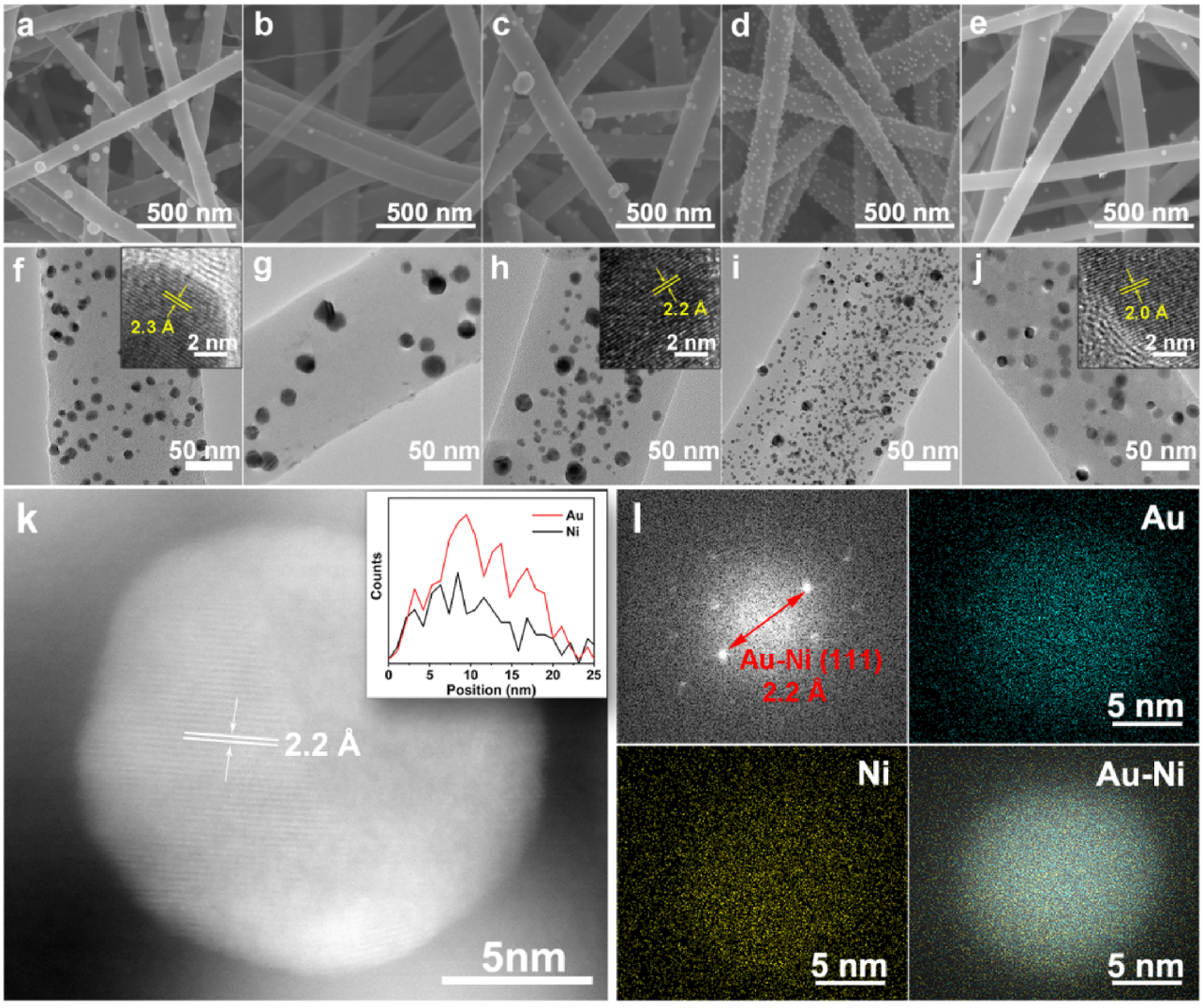

Fig. 1. FE-SEM and TEM images of (a, f) Au/CNFs, (b, g) Au_3Ni_1/CNFs, (c, h) Au_1Ni_1/CNFs, (d, i) Au_1Ni_3/CNFs (e, j) Ni/CNFs. The graphitization temperatures for all samples are 1000 °C. Insets in (f), (h) and (j) are the corresponding HRTEM images. (k) AC-HAADF-STEM image of Au_1Ni_1/CNFs. Inset in Fig. 1k is the line scan STEM-EDX spectra of the corresponding Au_1Ni_1 solid-solution alloy nanoparticles. (l) The corresponding fast Fourier transform (FFT) pattern and STEM-EDX elemental mapping images of Au_1Ni_1 NPs including the Au, Ni, and the mixed Au and Ni elements.

in accordance with the XRD data (2θ = 39.1°). The line scan STEM-EDX spectra of the Au_1Ni_1 solid-solution alloy NPs indicates that homogeneous distribution of Au and Ni elements. The total Au/Ni atomic molar ratio in CNFs collected by ICP-OES and X-ray photoelectron spectroscopy (XPS) was both about 1:1 (Table S1). A distinct *fcc* phase for the Au_1Ni_1 NPs can be confirmed by the fast fourier transform (FFT) pattern of Au_1Ni_1 NPs (Fig. 1l). The corresponding STEM-EDX elemental mappings of one Au_1Ni_1 NP display only one domain, further confirm the uniform distribution of Ni element throughout the homogeneous AuNi solid-solution alloy NPs. Low magnification STEM-EDX elemental mapping images confirmed the effective method for the large-scale synthesis of for Au_1Ni_1 homogeneous solid-solution alloy NPs (Fig. S4).

The surface chemical composition and electronic interaction of the prepared AuNi/CNFs were investigated by X-ray photoelectron spectroscopy (XPS). The XPS of Au/CNFs were investigated as control

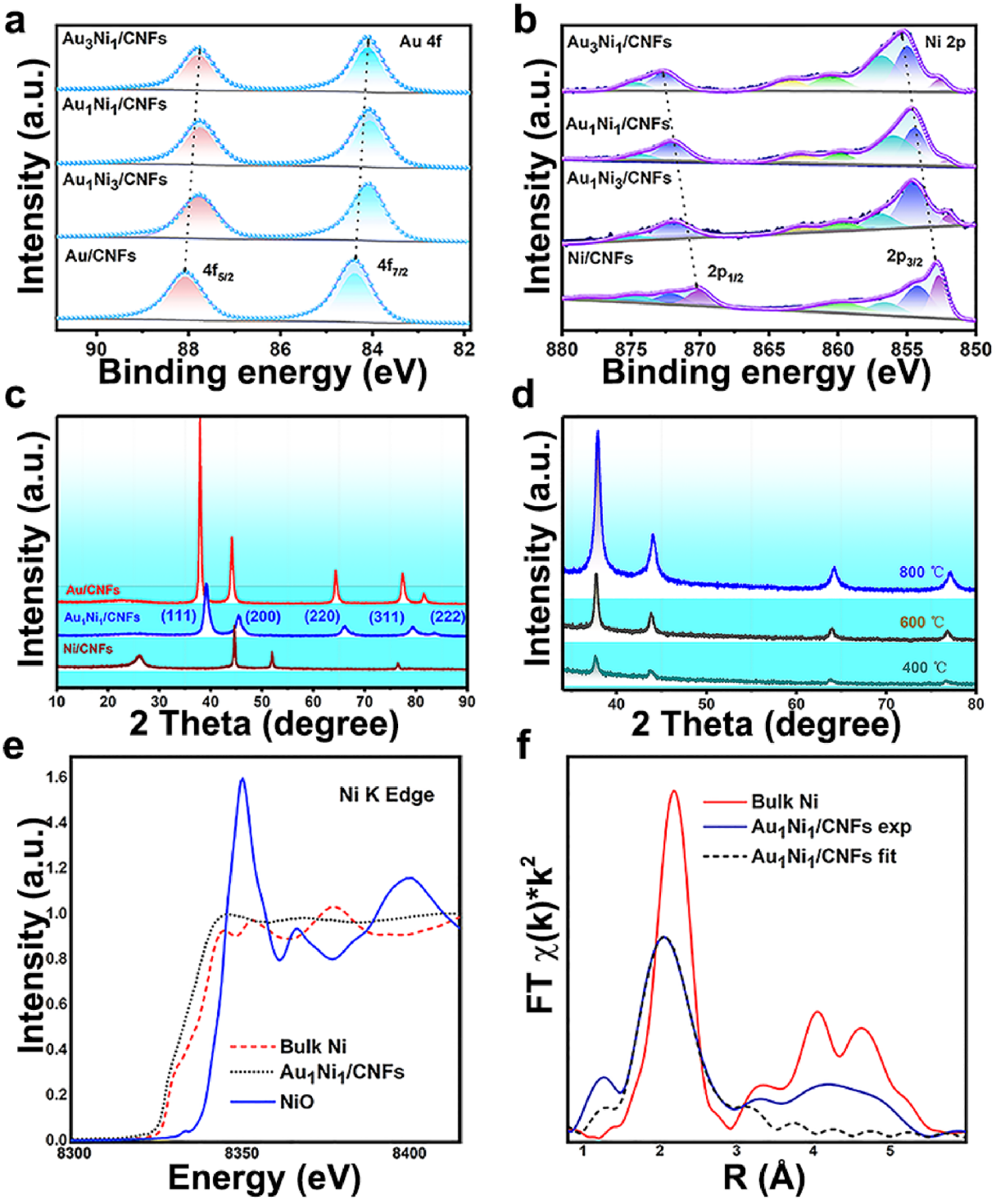

Fig. 2. Structure characterization of AuNi/CNFs. (a) Au 4f XPS spectra of Au/CNFs, Au_3Ni_1/CNFs, Au_1Ni_1/CNFs and Au_1Ni_3/CNFs. (b) Ni 2p XPS spectra of Ni/CNFs, Au_3Ni_1/CNFs, Au_1Ni_1/CNFs and Au_1Ni_3/CNFs. Dotted lines represent the calibration peak. (c) XRD patterns of the Au/CNFs, Au_1Ni_1/CNFs and Ni/CNFs. (d) *In situ* XRD patterns of Au_1Ni_1/CNFs with the temperature range from 400 to 800 ℃. (e) Normalized XANES spectra at the Ni *K*-edge of the Au_1Ni_1/CNFs with compared to Ni and NiO reference. (f) k^3–weighted Fourier transform EXAFS spectra in the R space of Au_1Ni_1/CNFs in comparison to Ni reference.

sample, and the binding energies (BEs) at 84.4 eV and 88.0 eV correspond to Au $4f_{7/2}$ and Au $4f_{5/2}$, respectively, thus confirming the existence of metallic Au^0 (Fig. 2a). With the formation of AuNi homogeneous alloy, the BEs of Au $4f_{7/2}$ and Au $4f_{5/2}$ for Au_3Ni_1/CNFs shift to 84.1 eV and 87.7 eV, respectively, indicating strong electronic interaction between Au and Ni atoms. Lower BEs of Au 4f for AuNi/CNFs demonstrate that the Au obtains electrons as alloying with Ni. Similarly, the XPS of Au_1Ni_1/CNFs and Au_1Ni_3/CNFs both exhibit the negative shifts in BEs for Au $4f_{7/2}$ and Au $4f_{5/2}$. The Ni 2p XPS spectra of the prepared samples were shown in Fig. 2b. The Ni/CNFs exhibit two pairs of the Ni 2p characteristic peaks, the BEs peaks of Ni $2p_{3/2}$ located at 852.8 eV, 854.4 eV and 855.8 eV, respectively, corresponding to the Ni^0, Ni^{2+} and Ni^{3+} ions. The high valences of Ni (Ni^{2+} and Ni^{3+}) inevitably existed in Ni/CNFs and AuNi/CNFs is attributed to the air oxidation of the Ni and AuNi NPs (Fig. 2b). The BEs for Ni $2p_{3/2}$ in Au_3Ni_1, Au_1Ni_1 and Au_1Ni_3 all exhibit the shifts to higher values, also suggesting the strong electronic interaction between Ni and Au atoms and the increased positively charged Ni center. Meanwhile, there is no evidence that Ni-C and Ni-N can contribute to the enhanced performance (Fig. S5).

The crystal structures of Au/CNFs, Ni/CNFs and AuNi/CNFs with different molar ratios of Au and Ni (Au_3Ni_1/CNFs, Au_1Ni_1/CNFs and Au_1Ni_3/CNFs) were investigated by the X-ray diffraction (XRD). As shown in Fig. 2c, the XRD pattern of Au/CNFs exhibits five characteristic peaks located at 2θ = 38.2°, 44.4°, 64.6°, 77.5° and 81.7°, corresponding to the (111), (200), (220), (311) and (222) planes of *fcc* Au crystals, respectively (JCPDS 04–0784). The XRD pattern of the Ni/CNFs shows the peaks at 2θ values of 44.6°, 51.9° and 76.5°,

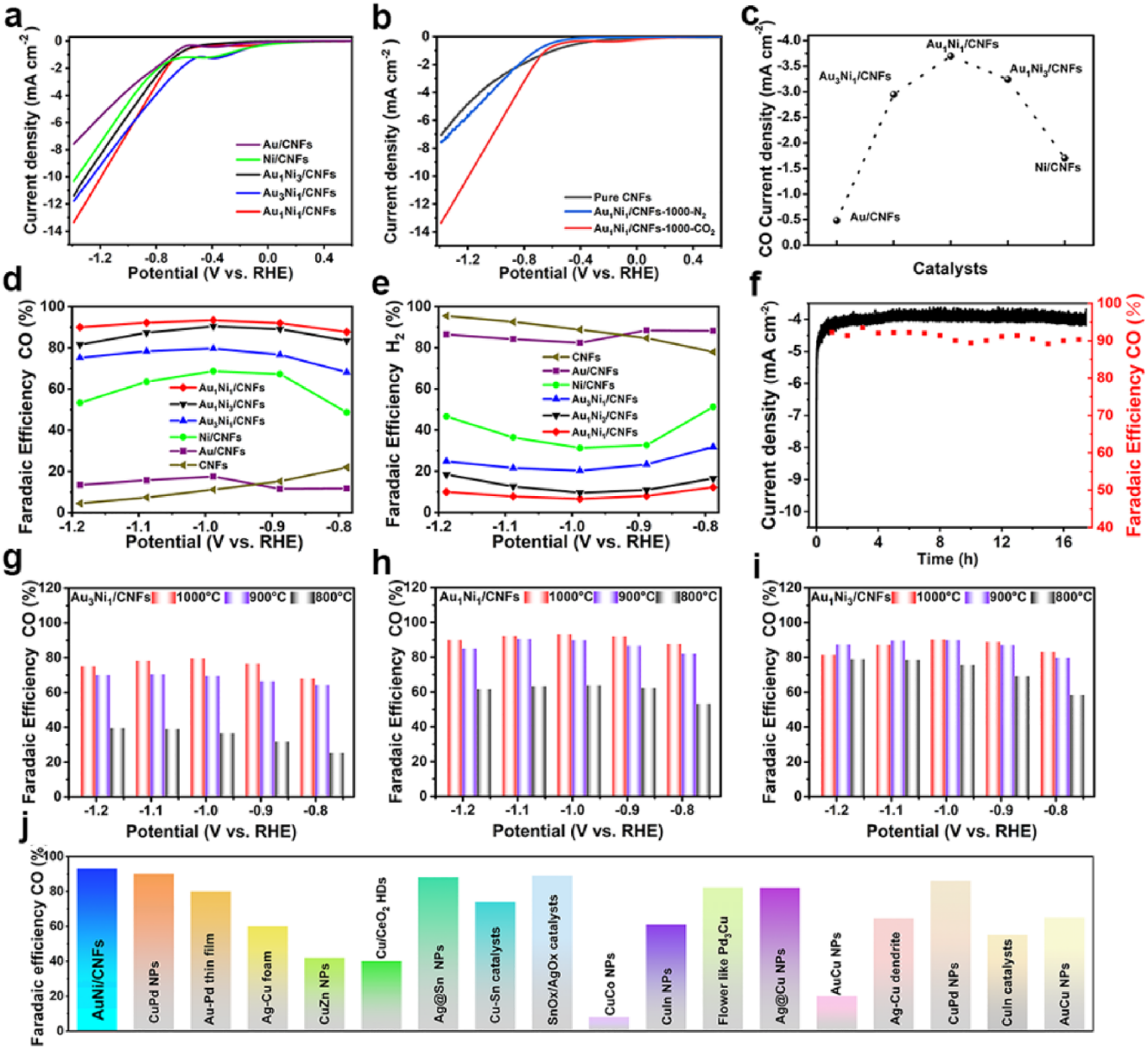

Fig. 3. CO_2RR performance of AuNi/CNFs samples. (a) LSV curves of Au/CNFs, Ni/CNFs and AuNi/CNFs in the potential range from 0.6 to −1.4 V vs. RHE. The graphitization temperatures for all samples are 1000 °C. (b) LSV curve of pure CNFs tested in 0.1 M CO_2 saturated $KHCO_3$, LSV curves of Au_1Ni_1/CNFs-1000 tested in 0.1 M CO_2 saturated $KHCO_3$ and 0.1 M N_2 saturated $KHCO_3$. (c) Variation tendency on current density of Au/CNFs, Ni/CNFs and AuNi/CNFs at −0.98 V vs. RHE. (d) FE of CO and (e) FE of H_2 for Au/CNFs, Ni/CNFs and AuNi/CNFs, each sample was tested three times and took the average. (f) The CO_2RR stability of Au_1Ni_1/CNFs-1000 under an overpotential of −0.98 V for > 16 h continuous experiment. FE of CO for (g) Au_3Ni_1/CNFs, (h) Au_1Ni_1/CNFs and (i) Au_1Ni_3/CNFs prepared at 800 °C, 900 °C and 1000 °C. The experimental deactivations on FE were shown in Table S4 and S5. (j) CO_2RR performance comparison of AuNi/CNFs and recently reported bimetallic CO_2RR electrocatalysts.

corresponding to the (111), (200) and (220) planes of Ni crystals, respectively (JCPDS 04–0850).

Compared with the Au/CNFs and Ni/CNFs, the Au_1Ni_1/CNFs show distinctly different XRD patterns, and the characteristic peaks occurred at $2\theta = 39.1^\circ$, 45.4°, 66.2°, 79.4° and 83.7°, respectively, indicating that new crystal phases of AuNi homogeneous solid-solution alloy formed. In a single region, the (111) peak of Au_1Ni_1 could be an indicator for the formation of new phase [26]. Otherwise, two kinds of XRD patterns from both metals can coexist [26,34]. As shown in Fig. S6, with the increased molar ratio of Ni, the peaks for AuNi alloy shift to higher values, suggesting the reduced lattice distances of AuNi alloy caused by alloying. In addition, for the XRD pattern of the Au_1Ni_3/CNFs, there is a small peak located at $2\theta = 51.45^\circ$, corresponding to the *fcc*-Ni phase. The results indicate that the excess molar ratio of Ni would lead to the formation of separated Ni phases. Fig. 2d shows the *in situ* XRD patterns of Au_1Ni_1/CNFs with temperatures from 400 to 800 °C. The XRD results indicate that the AuNi homogeneous alloy is formed at 400 °C. In addition, there were no other peaks emerged, suggesting the purity of AuNi homogeneous solid-solution alloy.

The superior performance of the AuNi solid-solution alloy cannot be interpreted by the simple alloy effects, thus the metallic nature of Ni was further confirmed by X-ray absorption near edge structure (XANES). As shown in Fig. 2e, the white line intensity of Au_1Ni_1/CNFs was slightly higher than that of bulk Ni, which might be due to the electron withdrawal effect of nearby Au atoms, since Au has stronger electronegativity comparing to Ni. This result is consistent with what we observed from XPS results that Ni is partially positively charged when alloying with Au. However, the white line intensity of Au_1Ni_1/CNFs was much lower than that of NiO, proving the absence of oxide Ni [35]. Besides, the typical shoulder peak at 8340 eV ascribed to Ni-N species was undetected, verifying the fact that there is no Ni-N bond in the AuNi/CNFs. The near edge structure with apparently different oscillation features also indicated the change of coordination environment after alloying, which could be fitted using ab initio method.

The first-shell simulation for Fourier-transform extended X-ray absorption fine structure (FT-EXAFS) of Au_1Ni_1/CNFs quantified the average coordination structure of Ni atoms (Fig. 2f). Fitting using both Ni-Ni and Ni-Au paths gave a better result than only using Ni-Ni path. The coordination number was 2.3 and 4.0 for Ni-Ni and Ni-Au, respectively (Table S2). It should be noted that the bonding distance of Ni-Au from fitting is quite same as what previously reported in an AuNi alloy system [36]. Besides, the lower shift peak around 2.0 Å can be ascribed to the formation of Au-Ni bond, in line with the reported reference [36]. And the decreased intensity of the peak further proves the coordination between Au and Ni. The absence of peak at 1.4 Å in AuNi/CNFs also confirms the no interaction between Ni and N atoms, indicating that the supported AuNi solid-solution alloy NPs may favor the enhanced CO_2RR performance other than the meal-nitrogen bond (M−N) as the crucial role. These results indicate that the successful formation of AuNi solid-solution alloy NPs can significantly improve the electronic interaction between Au and Ni.

3.2. CO_2 electroreduction performance

The electrocatalytic performance of Au/CNFs, Ni/CNFs and various AuNi/CNFs was conducted on a three-electrode system with a gas-hermetic H-cell reactor holding 0.1 M CO_2-saturated $KHCO_3$. The self-supported AuNi/CNFs were directly utilized as the working electrode for the experiment. The linear sweep voltammetry (LSV) curves for various AuNi/CNFs are shown in Fig. 3a. The applied potential was swept between 0.6 V and −1.4 V (vs. RHE) at a sweep rate of 50 mV s^{-1}. In addition, the geometrical current densities also contain HER current densities. As shown in Fig. 3a, compared with the poor CO_2RR activity of the individual Au/CNFs and Ni/CNFs, the geometrical current densities were enhanced with the formation of AuNi homogeneous alloy. Beyond that, the obvious enhancement in current density of Au_1Ni_1/CNFs-1000 tested in 0.1 M $KHCO_3$ saturated with CO_2 than that in N_2 reveals that the Au_1Ni_1/CNFs-1000 is more favorable for CO_2RR than HER and the source of CO product comes from CO_2 other than $KHCO_3$ (Fig. 3b). Besides, the supported AuNi homogeneous solid-solution alloy NPs play as the active sites in enhanced CO_2RR activity, evidenced by the low current density in LSV of pure CNFs. During the CO_2RR, Au_1Ni_1/CNFs-1000 indicates the largest current densities under the whole potential range as well (Fig. S7). Additionally, the main gaseous products were hydrogen (H_2) and carbon monoxide (CO) characterized by micro gas chromatography (GC). And there was no liquid product analyzed by ^{1}H NMR (Fig. S8 and S9). The Au_1Ni_1/CNFs show the highest CO current density of 4.0 mA cm^{-2} at −0.98 V (vs. RHE) in Fig. 3c, which is 1.1-fold, 1.08-fold, 1.5-fold and 1.7-fold relative to Au_1Ni_3/CNFs (3.6 mA cm^{-2}), Au_3Ni_1/CNFs (3.7 mA cm^{-2}), Au/CNFs (2.8 mA cm^{-2}) and Ni/CNFs (2.4 mA cm^{-2}), respectively. The increased Ni molar ratio in AuNi alloy would reduce the current density for CO_2 reduction, suggesting that the Ni alloying with Au could regulate the electronic structures of the Au and further improve the CO_2RR activity. However, the formation of Ni NPs in Au_1Ni_3/CNFs is due to excess molar ratio of Ni detected by XRD and XPS, which could decrease the geometrical current density (Fig. S7f). To understand the CO_2RR kinetics of Au_1Ni_1/CNFs-1000, Tafel plots were conducted (Fig. S10). Tafel slope of 159 mV dec^{-1} corresponding to the Au_1Ni_1/CNFs-1000 indicated that the step of CO_2 activation to *COOH determines the reaction rates on Au_1Ni_1/CNFs-1000 [10,37]. The introduction of Ni into Au can enhance the electron transfer from Au_1Ni_1/CNFs to CO_2.

Fig. 3d shows the FE_{CO} on various AuNi/CNFs electrodes from −0.78 V to −1.18 V (vs. RHE). The individual Au/CNFs obtain the FE_{CO} of 20% at −0.98 V, meanwhile, the Ni/CNFs show the FE_{CO} of 68%. Although Ni/CNFs present the moderate performance, it shows a poor stability (Fig. S11). The Au_1Ni_1/CNFs with the optimal FE_{CO} of 92% at −0.98 V is significantly higher than those of other catalysts in the full potential range from −0.78 to −1.18 V (vs. RHE). The optimal FE_{CO} values of Au_1Ni_3/CNFs and Au_3Ni_1/CNFs are 88% and 72% and the results indicate that the proportion of Ni in AuNi alloy has a significant promotion on the FE_{CO}. In addition, the FE_{CO} of Au_1Ni_1/CNFs maintains stable (> 90%), even at more negative potentials, suggesting an outstanding CO selectivity. On the other hand, Fig. 3e demonstrates that the FE of H_2 (Au/CNFs ≈ 82%, Au_1Ni_1/CNFs ≈ 9%) decreases with the increased Ni contents. It can be concluded that the change of electronic structure of AuNi homogeneous solid-solution alloy leads to a significant suppression with H_2 production. It is worth noting that the pure CNFs present higher activity for H_2 production than CO_2RR, indicative of the fact that the supported AuNi homogeneous solid-solution alloys NPs serve as the active sites for CO_2 reduction. Especially, the change of electronic structure in AuNi solid-solution alloy can be verified by the variation of CO_2RR activity as well as by XPS and XANES results. All the AuNi/CNFs catalysts achieve the maximum FE_{CO} at −0.98 V with the modest geometrical current density, while the total current density presents a monotonic increase with applied overpotential (Fig. S7). The electrochemical surface area (ECSA) values of as-prepared samples were measured by measuring double-layer capacitance (C_{dl}) from the scan rate dependence of cyclic voltammetry (CV) (Fig. S12). The highest ECSA value belongs to Au_1Ni_1/CNFs (6.54 mF cm^2). It should be mentioned that the long-term performance of Au_1Ni_1/CNFs-1000 conducted at −0.98 V presents negligible decay in the current density and FE during the continuous 16 h electrolysis. The XPS analysis of post Au_1Ni_1/CNFs shows that the ignorable BEs shift of Au 4f and Ni 2p, indicating the prepared catalysts were stable (Fig. S13).

Fig. 3g-i depict the FE_{CO} variation tendency of AuNi/CNFs prepared under temperatures from 800 to 1000 °C. The result demonstrates that the AuNi/CNFs-800 with FE_{CO} < 80% in the applied potential range is obviously inferior to those of AuNi/CNFs-900 and AuNi/CNFs-1000. Only a slight activity difference exists between AuNi/CNFs-900 and

AuNi/CNFs-1000 (FE_{CO} > 85%). Higher temperature can endow the catalysts with higher CO current density (Fig. S14) and ECSA (Fig. S15). It might be rationalized by that higher temperature may further facilitate the formation of AuNi single phase alloy through overcoming the immiscible limitation [26,32]. Thus, more homogeneous AuNi solid-solution alloy can benefit the enhanced CO_2RR activity. Notably, as shown in Fig. 3j and Table S3, the optimal FE_{CO} of AuNi/CNFs is compared with those of recently reported remarkable electrocatalysts. It is found that the AuNi/CNFs are competitive and significative among excellent CO_2RR catalysts including the AuCu, AuPd and AgCu and so on[10,14,18]. Besides, this effective synthetic method for the preparation of AuNi solid-solution alloy may promote the in-depth research of solid-solution alloy as CO_2RR catalysts.

3.3. CO_2 electroreduction mechanisms on Au_1Ni_1/CNFs

It has been widely accepted that the electroreduction of CO_2 to CO on transition metal surfaces via the following reaction pathway

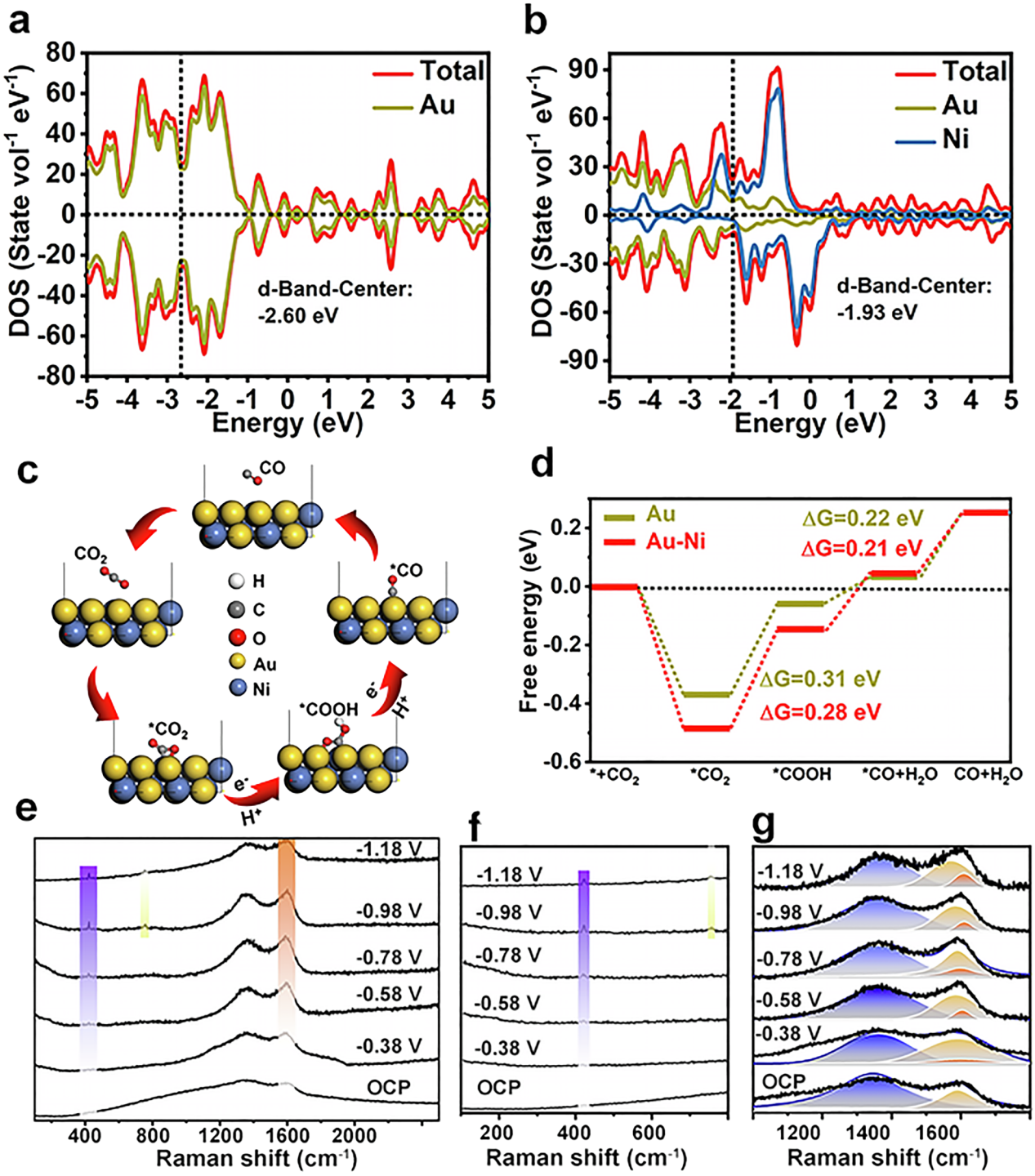

Fig. 4. Theoretical calculation of Au/CNFs and AuNi/CNFs for CO_2RR. Projected *d*-density of states (PDOS) of atoms on (a) Au (111) and (b) AuNi (111) surfaces. (c) Schematic of the reaction steps of electroreduction CO_2 to CO. (d) DFT calculations. Free energy diagrams for CO_2RR pathways on Au (111) and AuNi (111) model catalyst surface. (e–g) Potential-dependent operando Raman spectroscopy of Au_1Ni_1/CNFs-1000 in the potential range from open potential circuit (OCP) to −1.18 V vs. RHE.

[10,19], where * represents adsorption sites.

$CO_2 + * \rightarrow *CO_2$(1)

$*CO_2 + H^+ + e^- \rightarrow *COOH$(2)

$*COOH + H^+ + e^- \rightarrow *CO + H_2O$(3)

$*CO \rightarrow CO + *$(4)

To further illustrate the relationship between the electronic structure of AuNi homogeneous solid-solution alloy catalysts and the activity of intermediates during CO_2 to CO, the projected density of states (PDOS) of Au and AuNi homogeneous solid-solution alloy were calculated. As observed in Fig. 4a-b, more positive *d*-band center of AuNi (1 1 1) was obtained by the incorporation of Ni into Au compared with Au (1 1 1) by 0.67 eV. It is consistent with the results of XANES and XPS valence band spectra (Fig. S16) of Au/CNFs and Au_1Ni_1/CNFs. Besides, more electron density could be introduced at the Fermi level of 0 eV. More positive *d*-band center and more electron density at Fermi level of 0 eV can tune the binding energies and strong interactions between metal and intermediates of CO_2RR, which can be estimated from the interpolation principle, improving the CO selectivity ultimately [38].

DFT calculation was conducted to further investigate on the role of Ni from AuNi homogeneous solid-solution alloy in tuning the electronic structure of homogeneous AuNi solid-solution alloy as well as the CO_2RR performance. The optimal configuration of reactant, intermediates and products on the Au and AuNi surface are presented in Fig. 4c. Further, the DFT calculations on the elementary reaction steps of CO_2 reduction to CO on Au NPs and AuNi NPs are shown in Fig. 4d, the superior CO_2RR activity of AuNi alloy compared to pure Au NPs can be observed. Firstly, the adsorption of CO_2 (Step 1) on the surface of catalysts is the initial process of the CO_2 activation [10]. A downhill energy barrier along with $*CO_2$ and *COOH formation can be observed, meaning that this step can be facilely taken place on Au (1 1 1) and AuNi (1 1 1). However, Fig. 4d reveals that the formation of intermediates $*CO_2$ on AuNi (1 1 1) with a free energy barrier of 0.49 eV compared to Au (1 1 1) (ΔG = 0.38 eV), thus indicating the introduction of Ni into Au can facilitate the adsorption of CO_2 during the CO_2RR. Especially, the elementary step of the CO_2 activation to *COOH (Step 2) is regarded as the rate-determining step (RDS) toward CO_2 reduction to CO on AuNi/CNFs. The *COOH formation on AuNi (1 1 1), which is the first proton coupled electron-transfer step, presents the more negative free energy than that on Au (1 1 1), and only a smaller free energy barrier (ΔG = 0.28 eV) can meet the formation of *COOH on AuNi (1 1 1). After the formation of adsorbed *COOH, the second proton-coupled electron transfer step with *CO formation on Au (1 1 1) and AuNi (1 1 1) presented uphill free-energy pathways. It should be pointed out that the free energy change for the *CO formation increases on AuNi (1 1 1) than that on Au (1 1 1). Combined with the experimental data, the Au (1 1 1) may suffer from CO poisoning, resulting in a lower CO FE of Au/CNFs. However, the CO desorption on AuNi (1 1 1), which is uphill in energy by (ΔG = 0.21 eV) lower than that (ΔG = 0.22 eV) on Au (1 1 1), indicating that the introduction of Ni into Au can benefit the CO desorption from AuNi (1 1 1).

Generally, it needs relatively high energy barriers for the activation of CO_2 to *COOH and the desorption of CO [10]. The DFT calculation demonstrates that the prepared AuNi homogeneous solid-solution alloy can significantly reduce the free energy barriers for these two steps. Based on the result of DFT calculations, more positive *d*-band center is obtained as the incorporation of Ni. It can be concluded that the adsorption of CO_2 and desorption of CO are facilitated on the AuNi solid-solution alloy due to the presence of AuNi electronic interaction, which results in the significantly improved CO_2RR activity compared with that of pure metal catalysts.

In order to support the conclusion on reduced free energy barrier for the CO_2 activation and *CO desorption caused by the incorporation of Ni into Au, the *Operando* Raman spectroscopy of Au/CNFs-1000, Ni/CNFs-1000 and Au_1Ni_1/CNFs-1000 was performed using a spectro-electrochemical cell. As shown in Fig. 4e, the original catalyst shows no characteristic peaks belong to the metal, and no significant shifts on the main peaks were characterized. An increased peak (420 cm^{-1}) can be observed when the potential applied to Au_1Ni_1/CNFs-1000 is stepped negatively from −0.58 V to −0.98 V vs. RHE. Meanwhile, compared with pure Au/CNFs and Ni/CNFs, there is a clear difference emerged in AuNi/CNFs, presenting a significantly increased intensity of this peak (Fig. S17). After −0.98 V, the intensity of this peak becomes slightly decreased, which is consistent with the tendency of FE_{CO} on Au_1Ni_1/CNFs. Combined with literature and the DFT process of CO production, this peak could come from the metal-adsorbate stretching vibration of linear C═O band (AuNi-CO_L) [38,39]. Note that the increased intensity of peak (1590 cm^{-1}) contrasted to the peak of disorder carbon (1350 cm^{-1}) from OCP to −1.18 V, which generally belongs to graphite carbon. This activity could be rationalized by the higher abundance of the adsorbed carboxyl species (the $*CO_2^-$) that is regarded as an intermediate for CO production on Au_1Ni_1/CNFs-1000 [40,41]. Further, the weak peaks around 730 cm^{-1} at −0.98 V- −1.08 V vs. RHE are in good agreement with the in plane bending vibrations (δCO_2^-), another vibrational mode of $*CO_2^-$ reported by related literature [41]. Meanwhile, for Au/CNFs-1000 and Ni/CNFs-1000 (Fig. S17), the peaks attributed to *COOH are absent with the potential range from OCP to −0.98 V. This characteristic feature of the Au_1Ni_1/CNFs complies well with a CO_2RR where the *COOH formation is characterized as the RDS by DFT and Tafel analysis. Additionally, the results demonstrate that the Au_1Ni_1 homogeneous solid-solution alloy with positively charged Ni center can facilitate the activation of CO_2 into *COOH and enhance the interaction between *COOH and AuNi (1 1 1) due to the change of electronic structure.

4. Conclusions

In conclusion, the AuNi homogeneous solid-solution alloy NPs with positively charged Ni center on CNFs has been prepared via facile electrospinning and graphitization process, serving as CO_2RR catalyst with high selectivity. The Au_1Ni_1/CNFs catalyst (graphitization temperature is 1000 ℃) presented the optimal FE_{CO} = 92% at −0.98 V vs RHE, lowest overpotential for CO_2RR and highest current density when compared to pure Au and Ni NPs. The enhanced catalytic performance strong depends on the electronic structure of AuNi homogeneous solid-solution alloy. XAFS demonstrates the positively charged Ni center in AuNi solid-solution alloy and the strong interaction between Au and Ni atoms, confirming the formation of homogeneous AuNi solid-solution alloy. DFT calculations indicate that the incorporation of Ni into Au can make the *d*-band center more positive and reduce the free energy barrier for the CO_2 activation into *COOH and *CO desorption. Operando Raman spectroscopy provides the evidences that AuNi homogeneous solid-solution alloy with positively charged Ni center can facilitate the activation of CO_2 into *COOH and enhance the interaction between *COOH and AuNi (1 1 1) due to the change of electronic structure. This work not only offers fundamental understanding between electronic structure and free energy of elementary steps of CO_2RR, but also provides a new strategy for designing the homogeneous solid-solution alloy as highly efficient CO_2RR catalyst.

Declaration of Competing Interest

The authors declare that they have no known competing financial interests or personal relationships that could have appeared to influence the work reported in this paper.

Acknowledgments

This study was supported by the National Natural Science Foundation of China (NSFC) (grant nos. 51803077), Natural Science

Foundation of Jiangsu Province (grant nos. BK20180627), Postdoctoral Science Foundation of China (2018M630517, 2019T120389), the MOE & SAFEA, 111 Project (B13025), the national first-class discipline program of Light Industry Technology and Engineering (LITE2018-19), the Fundamental Research Funds for the Central Universities.

Appendix A. Supplementary data

Supplementary data to this article can be found online at https://doi.org/10.1016/j.cej.2020.126523.

References

[1] C.S. Diercks, Y. Liu, K.E. Cordova, O.M. Yaghi, The role of reticular chemistry in the design of CO_2 reduction catalysts, Nat. Mater. 17 (2018) 301–307.
[2] J.H. Lee, S. Kattel, Z. Jiang, Z. Xie, S. Yao, B.M. Tackett, W. Xu, N.S. Marinkovic, J.G. Chen, Tuning the activity and selectivity of electroreduction of CO_2 to synthesis gas using bimetallic catalysts, Nat. Commun. 10 (2019) 3724.
[3] M. Jia, C. Choi, T.S. Wu, C. Ma, P. Kang, H. Tao, Q. Fan, S. Hong, S. Liu, Y.L. Soo, Y. Jung, J. Qiu, Z. Sun, Carbon-supported Ni nanoparticles for efficient CO_2 electroreduction, Chem. Sci. 9 (2018) 8775–8780.
[4] Q. Cheng, K. Mao, L. Ma, L. Yang, L. Zou, Z. Zou, Z. Hu, H. Yang, Encapsulation of iron nitride by Fe–N–C shell enabling highly efficient electroreduction of CO_2 to CO, ACS Energy Lett. 3 (2018) 1205–1211.
[5] H.-Y. Jeong, M. Balamurugan, V.S.K. Choutipalli, E.-S. Jeong, V. Subramanian, U. Sim, K.T. Nam, Achieving highly efficient CO_2 to CO electroreduction exceeding 300 mA cm^{-2} with single-atom nickel electrocatalysts, J. Mater. Chem. A 7 (2019) 10651–10661.
[6] K. Sun, T. Cheng, L. Wu, Y. Hu, J. Zhou, A. Maclennan, Z. Jiang, Y. Gao, W.A. Goddard III, Z. Wang, Ultrahigh mass activity for carbon dioxide reduction enabled by gold-iron core-shell nanoparticles, J. Am. Chem. Soc. 139 (2017) 15608–15611.
[7] P. Moreno-García, N. Schlegel, A. Zanetti, A. Cedeño López, M.A.D. J.S. Gálvez-Vázquez, A. Dutta, M. Rahaman, P. Broekmann, Selective electrochemical reduction of CO_2 to CO on Zn-based foams produced by Cu^{2+} and template-assisted electrodeposition, ACS Appl. Mater. Interfaces 10 (2018) 31355–31365.
[8] J. Gu, C.-S. Hsu, L. Bai, H.M. Chen, X. Hu, Atomically dispersed Fe^{3+} sites catalyze efficient CO_2 electroreduction to CO, Science 364 (2019) 1091–1094.
[9] W. Zhu, R. Michalsky, Ö. Metin, H. Lv, S. Guo, C.J. Wright, X. Sun, A.A. Peterson, S. Sun, Monodisperse Au nanoparticles for selective electrocatalytic reduction of CO_2 to CO, J. Am. Chem. Soc. 135 (2013) 16833–16836.
[10] S. Zhu, Q. Wang, X. Qin, M. Gu, R. Tao, B.P. Lee, L. Zhang, Y. Yao, T. Li, M. Shao, Tuning structural and compositional effects in Pd-Au nanowires for highly selective and active CO_2 electrochemical reduction reaction, Adv. Energy Mater. 8 (2018) 1802238.
[11] J. Rosen, G.S. Hutchings, Q. Lu, S. Rivera, Y. Zhou, D.G. Vlachos, F. Jiao, Mechanistic insights into the electrochemical reduction of CO_2 to CO on nanostructured Ag surfaces, ACS Catal. 5 (2015) 4293–4299.
[12] A.M. Ismail, G.F. Samu, Á. Balog, E. Csapó, C. Janáky, Composition-dependent electrocatalytic behavior of Au–Sn bimetallic nanoparticles in carbon dioxide reduction, ACS Energy Lett. 4 (2018) 48–53.
[13] W. Ren, X. Tan, W. Yang, C. Jia, S. Xu, K. Wang, S.C. Smith, C. Zhao, Isolated diatomic Ni-Fe metal-nitrogen sites for synergistic electroreduction of CO_2, Angew. Chem. Int. Ed. 58 (2019) 6972–6976.
[14] H. Zhang, J. Wang, Z. Zhao, H. Zhao, M. Cheng, A. Li, C. Wang, J. Wang, J. Wang, The synthesis of atomic Fe embedded in bamboo-CNTs grown on graphene as a superior CO_2 electrocatalyst, Green Chem. 20 (2018) 3521–3529.
[15] S. Zhu, X. Qin, Q. Wang, T. Li, R. Tao, M. Gu, M. Shao, Composition-dependent CO_2 electrochemical reduction activity and selectivity on Au–Pd core–shell nanoparticles, J. Mater. Chem. A 7 (2019) 16954–16961.
[16] A. Zhang, Y. Liang, H. Li, X. Zhao, Y. Chen, B. Zhang, W. Zhu, J. Zeng, Harmonizing the electronic structures of the adsorbate and catalysts for efficient CO_2 reduction, Nano Lett. 19 (2019) 6547–6553.
[17] N. Wu, L. Xiao, L. Zhuang, Theoretical search for novel Au or Ag bimetallic alloys capable of transforming CO_2 into hydrocarbons, J. Mater. Chem. A 7 (2019) 20567–20573.
[18] Z. Yin, D. Gao, S. Yao, B. Zhao, F. Cai, L. Lin, P. Tang, P. Zhai, G. Wang, D. Ma, Highly selective palladium-copper bimetallic electrocatalysts for the electrochemical reduction of CO_2 to CO, Nano Energy 27 (2016) 35–43.
[19] D. Kim, J. Resasco, Y. Yu, A.M. Asiri, P. Yang, Synergistic geometric and electronic effects for electrochemical reduction of carbon dioxide using gold-copper bimetallic nanoparticles, Nat. Commun. 5 (2014) 4948.
[20] F. Wang, K. Kusada, D. Wu, T. Yamamoto, H. Kitagawa, Solid-Solution Alloy Nanoparticles of the Immiscible Ir-Cu System with a wide composition range for enhanced electrocatalytic applications, Angew. Chem. Int. Ed. 57 (2018) 4505–4509.
[21] K. Jiang, S. Siahrostami, T. Zheng, Y. Hu, S. Hwang, E. Stavitski, Y. Peng, J. Dynes, M. Gangisetty, D. Su, K. Attenkofer, H. Wang, Isolated Ni single atoms in Graphene nanosheets for high-performance CO_2 reduction, Energy Environ. Sci. 11 (2018) 893–903.
[22] H. Okamoto, Desk Handbook: Phase Diagrams For Binary Alloys, ASM international, Materials Park, USA, 2000.
[23] H. You, S. Yang, B. Ding, H. Yang, Synthesis of colloidal metal and metal Alloy nanoparticles for electrochemical energy applications, Chem. Soc. Rev. 42 (2013) 2880–2904.
[24] P.C. Chen, G. Liu, Y. Zhou, K.A. Brown, N. Chernyak, J.L. Hedrick, S. He, Z. Xie, Q.Y. Lin, V.P. Dravid, S.A. O'Neill-Slawecki, C.A. Mirkin, Tip-directed synthesis of multimetallic nanoparticles, J. Am. Chem. Soc. 137 (2015) 9167–9173.
[25] D. Liang, G. Zangari, Underpotential codeposition of Au-Ni alloys: the influence of applied potential on phase separation and microstructure, J. Electrochem. Soc. 163 (2016) D3020–D3026.
[26] S. Zou, P. Qiao, D. Zhang, Y. Yan, J. Liu, J. Li, L. Xiao, J. Fan, Fabricating the AuPdPt ternary nanophase diagram at 800 °C to guide the exploration of optimal catalyst for n-hexane oxidation, J. Phys. Chem. C 121 (2017) 4074–4082.
[27] Y. Yao, Z. Huang, P. Xie, S.D. Lacey, R.J. Jacob, H. Xie, F. Chen, A. Nie, T. Pu, M. Rehwoldt, Carbothermal shock synthesis of high-entropy-alloy nanoparticles, Science 359 (2018) 1489–1494.
[28] W. Sheng, S. Kattel, S. Yao, B. Yan, Z. Liang, C.J. Hawxhurst, Q. Wu, J.G. Chen, Electrochemical reduction of CO_2 to synthesis gas with controlled CO/H_2 ratios, Energy Environ. Sci. 10 (2017) 1180–1185.
[29] Y. Deng, L.R.L. Ting, P.H.L. Neo, Y.-J. Zhang, A.A. Peterson, B.S. Yeo, Operando Raman spectroscopy of amorphous molybdenum sulfide (MoS_x) during the electrochemical hydrogen evolution reaction: Identification of sulfur atoms as catalytically active sites for H^+ reduction, ACS Catal. 6 (2016) 7790–7798.
[30] T. Tsukamoto, T. Kambe, A. Nakao, T. Imaoka, K. Yamamoto, Atom-hybridization for synthesis of polymetallic clusters, Nat. Commun. 9 (2018) 3873.
[31] B. Ni, P. He, W. Liao, S. Chen, L. Gu, Y. Gong, K. Wang, J. Zhuang, L. Song, G. Zhou, X. Wang, Surface oxidation of AuNi heterodimers to achieve high activities toward hydrogen/oxygen evolution and oxygen reduction reactions, Small 14 (2018) e1703749.
[32] W. Yi, W. Yuan, Y. Meng, S. Zou, Y. Zhou, W. Hong, J. Che, M. Hao, B. Ye, L. Xiao, Y. Wang, H. Kobayashi, J. Fan, A rational solid-state synthesis of supported Au-Ni bimetallic nanoparticles with enhanced activity for gas-phase selective oxidation of alcohols, ACS Appl. Mater. Interfaces 9 (2017) 31853–31860.
[33] H. Lv, Z. Xi, Z. Chen, S. Guo, Y. Yu, W. Zhu, Q. Li, X. Zhang, M. Pan, G. Lu, S. Mu, S. Sun, A new core/shell NiAu/Au nanoparticle catalyst with Pt-like activity for hydrogen evolution reaction, J. Am. Chem. Soc. 137 (2015) 5859–5862.
[34] J.F. Bondi, R. Misra, X. Ke, I.T. Sines, P. Schiffer, R.E. Schaak, Optimized synthesis and magnetic properties of intermetallic Au_3Fe_{1-x}, Au_3Co_{1-x}, and Au_3Ni_{1-x} nanoparticles, Chem. Mater. 22 (2010) 3988–3994.
[35] Y. Chin, D. King, H. Roh, Y. Wang, S. Heald, Structure and reactivity investigations on supported bimetallic AuNi catalysts used for hydrocarbon steam reforming, J. Catal. 244 (2006) 153–162.
[36] S. Shirakawa, M. Osaki, Y. Nagai, Y.F. Nishimura, K. Dohmae, S.I. Matsumoto, H. Hirata, XAFS study on promoting effect of Au via NiO reduction in Au-Ni bimetallic clusters, Catal. Today 281 (2017) 429–436.
[37] R. Kortlever, J. Shen, K.J. Schouten, F. Calle-Vallejo, M.T. Koper, Catalysts and reaction pathways for the electrochemical reduction of carbon dioxide, J. Phys. Chem. Lett. 6 (2015) 4073–4082.
[38] P. Zhang, J. Cai, Y.-X. Chen, Z.-Q. Tang, D. Chen, J. Yang, D.-Y. Wu, B. Ren, Z.-Q. Tian, Potential-dependent chemisorption of carbon monoxide at a gold core-platinum shell nanoparticle electrode: A combined study by electrochemical in situ surface-enhanced Raman spectroscopy and density functional theory, J. Phys. Chem. C 114 (2009) 403–411.
[39] S. Jiang, K. Klingan, C. Pasquini, H. Dau, New aspects of operando Raman spectroscopy applied to electrochemical CO_2 reduction on Cu foams, J. Chem. Phys. 150 (2019) 041718.
[40] I.V. Chernyshova, P. Somasundaran, S. Ponnurangam, On the origin of the elusive first intermediate of CO_2 electroreduction, Proc. Natl. Acad. Sci. U. S. A. 115 (2018) E9261–E9270.
[41] A. Vasileff, X. Zhi, C. Xu, L. Ge, Y. Jiao, Y. Zheng, S.-Z. Qiao, Selectivity control for electrochemical CO_2 reduction by charge redistribution on the surface of copper alloys, ACS Catal. 9 (2019) 9411–9417.